Fermi surface reconstruction due to orthorhombic distortion in the Dirac semimetal $YbMnSb_2$

Dilip Bhoi,[1,*] Feng Ye,[2] Hanming Ma,[1] Xiaoling Shen,[1] Arvind Maurya,[3] Shusuke Kasamatsu,[4] Takahiro Misawa,[1] Kazuyoshi Yoshimi,[1] Taro Nakajima,[1] Masaki Kondo,[1] Yuto Kinoshita,[1] Masashi Tokunaga,[1] Masaaki Matsuda,[2] and Yoshiya Uwatoko[1]

[1]*The Institute for Solid State Physics, University of Tokyo, Kashiwa, Chiba 277-8581, Japan*
[2]*Neutron Scattering Division, Oak Ridge National Laboratory, Oak Ridge, Tennessee 37831, USA*
[3]*Department of Physics, School of Physical Sciences, Mizoram University, Aizawl 796 004, India*
[4]*Academic Assembly (Faculty of Science), Yamagata University, Yamagata 990-8560, Japan*

(Received 22 June 2023; revised 27 March 2025; accepted 27 May 2025; published 20 June 2025)

A Dirac semimetal with magnetic atoms as constituents delivers an interesting platform to investigate the interplay of Fermi surface (FS) topology, electron correlation, and magnetism. One such family of semimetals is $YbMnPn_2$ (Pn = Sb, Bi), which is being actively studied due to the intertwined spin and charge degrees of freedom. Here, we investigate the relationship between the magnetic/crystal structures and FS topology of $YbMnSb_2$ using single crystal x-ray diffraction, neutron scattering, magnetic susceptibility, magnetotransport measurements, and complimentary density functional theory (DFT) calculations. Contrary to previous reports, the x-ray and neutron diffraction reveal that $YbMnSb_2$ crystallizes in an orthorhombic *Pnma* structure with a notable antiphase displacement of the magnetic Mn ions that increases in magnitude upon cooling. As a result of this orthorhombicity, first-principles DFT calculation reveals a reduced Brillouin zone and more anisotropic FS of $YbMnSb_2$ compared to $YbMnBi_2$. Moreover, the hole-type carrier density drops by two orders of magnitude as $YbMnSb_2$ orders antiferromagnetically, indicating band folding in a magnetic ordered state. In addition, the Landau level fan diagram yields a nontrivial nature of the Shubnikov–de Haas quantum oscillation frequency arising from the Dirac-like Fermi pocket. These results imply that $YbMnSb_2$ is an ideal platform to explore the interplay of subtle lattice distortion, magnetic order, and topological transport arising from relativistic quasiparticles.

DOI: 10.1103/lk8w-7hkj

I. INTRODUCTION

Magnetic Dirac/Weyl semimetals deliver a promising platform, where the novel coupling between magnons and relativistic fermions could be exploited to manipulate the quantum transport phenomena using various parameters such as chemical substitution, pressure, strain, etc. In this context, the collinear antiferromagnetic (AFM) ternary $AMnPn_2$ (where A = rare earth elements such as Eu, Yb or alkali earth elements such as Ca, Sr, Ba; Pn = pnictides Sb or Bi) have attracted increasing attention due to the presence of anisotropic Dirac cones close to the Fermi level, E_F [1–16].

The 112-type $AMnPn_2$ consists of a stacking of two-dimensional (2D) Pn conduction layers, A layers, and insulating $MnPn_4$ layers as shown in Fig. 1(a). In $MnPn_4$ layers, each Mn atom is surrounded by four Pn atoms forming a tetrahedron, whereas two-dimensional (2D) Pn layers are responsible mostly for exotic properties such as quantum magnetoresistance [1–6] and the bulk quantum Hall effect [16–18]. Band structure calculations revealed that the electronic density of states at E_F is primarily composed of Pn-$p_{x/y}$ and Mn-d orbitals, suggesting a close relationship between the Mn moment direction and underlying electronic structure [19–23]. Interestingly, these calculations further predict that the ferromagnetic (FM) component arising from a canting of Mn moments breaks the time-reversal symmetry, thus playing a vital role in producing different topological states depending on the Mn moment direction [15,19–24].

Among the 112 materials, $YbMnPn_2$ are particularly unique due to the coupling between magnetism and Dirac quasiparticles [25–28], unusual interlayer quantum coherent transport [5,29], including promising attributes required for energy conversion technologies such as large thermoelectric power [30,31] and a giant anomalous Nernst effect [19,32]. Band structure calculations [19,20,23,29,30,33] identified $YbMnBi_2$ and $YbMnSb_2$ as nodal line semimetals, where the Fermi surface (FS) consists of two Dirac-like bands and a heavy 3D parabolic band. Despite these results pointing to similar FS topology, experiments indicate differences between the FSs of the two compounds. Quantum oscillation studies [5,6] in $YbMnBi_2$ detected two frequencies with a Dirac-like dispersion and a large carrier density ($\sim 10^{21}$ cm^{-3}) comparable to other Weyl semimetals such as Cd_3As_2 and NbP. In contrast, the observation of a single quantum oscillation frequency [29,34] and two orders of magnitude smaller carrier density [29,30,34] in $YbMnSb_2$ is difficult to reconcile within existing theoretical results.

In this work, we have used neutron and x-ray diffraction to characterize the proper magnetic and crystal structures of $YbMnSb_2$ and investigate the correlation between the crystal/magnetic structures and FS topology via magnetic

*Present address: Department of Engineering Science, University of Electro-Communications, Chofu, Tokyo 182-8585, Japan.

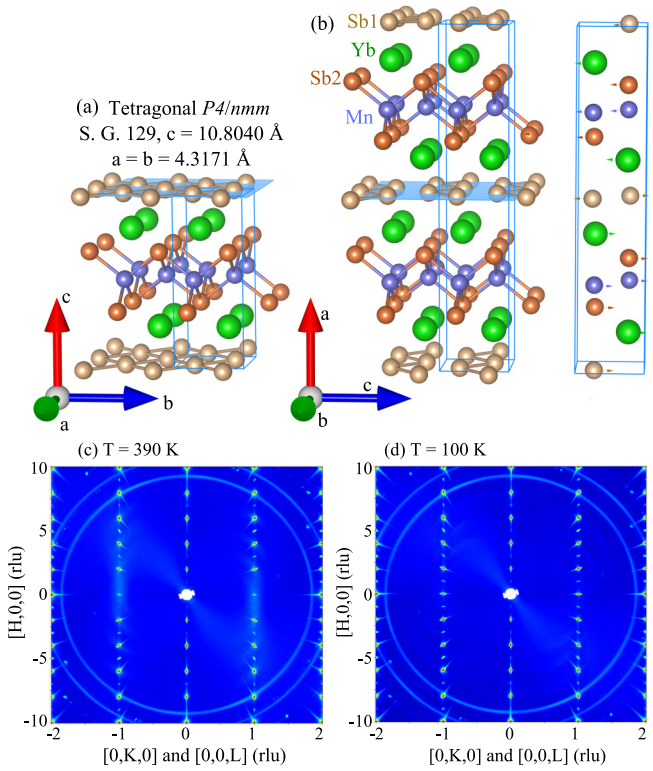

FIG. 1. (a) The reported tetragonal $P4/nmm$ crystal structure of $YbMnSb_2$ as in Refs. [27–31,33,34,38]. (b) The orthorhombic *Pnma* structure reported in this work. Arrows show the displacements of each atom along the a axis of the tetragonal $P4/nmm$ structure. The blue-shaded regions illustrate the Sb_1 layers. Blue rectangles highlight the unit cell. The contour plot of the neutron scattering intensity pattern of $YbMnSb_2$ at (c) $T = 390$ K and (d) $T = 100$ K in the $(H, K, 0)$ and $(H, 0, L)$ planes using the lattice parameters (21.58 Å, 4.3 Å, 4.3 Å).

susceptibility, magnetotransport measurements, and first-principles calculations. We have identified that $YbMnSb_2$ crystallizes in an orthorhombic *Pnma* structure with a notable antiphase displacement between the neighboring layers of the magnetic Mn ions. A band structure calculation, utilizing the newly obtained structural parameters, yields a reduced Brillouin zone (BZ) and more anisotropic FS topology of $YbMnSb_2$ than the Bi-based sister compound.

II. EXPERIMENTAL METHODS AND TECHNIQUE

We have prepared large single crystals of $YbMnSb_2$ using antimony as a flux. The high-purity elements of Yb, Mn, and Sb with a 1:1:4 stoichiometric ratio were placed in an alumina crucible as the starting materials. To grow the single crystals we followed the recipe as described in Ref. [29]. The as-grown single crystals were extensively characterized by single crystal x-ray and neutron diffraction at room temperature and an energy dispersive x-ray analysis (EDX). To check the chemical homogeneity of the crystal, EDX spectra obtained at several randomly selected spots from the samples were analyzed. The analyses show that the crystals are chemically homogeneous within the limit of EDX with an average stoichiometric ratio, Yb : Mn : Sb = 0.98 : 1.01 : 2.01.

A rectangular piece of $YbMnSb_2$ single crystal was cut for magnetic susceptibility measurements in a superconducting quantum interference device (MPMS XL, Quantum Design). Electrical resistivity and heat capacity measurements in the temperature range between 2 and 390 K were performed using a Quantum Design physical property measurement system. For Shubnikov–de Hass quantum oscillation measurements up to 16 T an Oxford superconducting magnet was used, while measurements up to 35 T were carried out using a nondestructive pulse magnet at The Institute for Solid State Physics, University of Tokyo.

Neutron diffraction measurements were performed on the time-of-flight neutron diffractometer CORELLI installed at SNS in the Oak Ridge National Laboratory (ORNL), USA using a piece of single crystal with a weight of ∼100 mg. The single crystal was cooled down using a closed-cycle refrigerator. Data reduction and analysis were conducted using MANTID software [35]. Magnetic structures were analyzed with SARAH software [36]. All the refinements of the neutron scattering data were performed with FULLPROF software [37]. The polarized neutron scattering measurements were performed at the polarized neutron triple-axis spectrometer PONTA installed at JRR-3 in the Japan Atomic Energy Agency, Japan and polarized neutron triple-axis spectrometer PTAX installed at HFIR in ORNL. The spectrometer was operated in the P_{xx} longitudinal polarization analysis mode, in which the direction of the neutron spin polarization was set to be parallel or antiparallel to the scattering vector, Q $(= k_i - k_f)$, by guide fields and a spin flipper.

III. RESULTS AND DISCUSSION

Earlier studies [27–31,33,34,38] reported that $YbMnSb_2$ has a layered tetragonal $P4/nmm$ structure [Fig. 1(a)]. However, the neutron scattering studies of the $YbMnSb_2$ single crystal taken at $T = 300$ K clearly show the presence of notable reflections which should be absent in the tetragonal $P4/nmm$ space group [38]. The origin of those forbidden reflections was not identified, partly due to the limited observable peaks. To reveal the proper crystal structure, we use the white beam neutron diffractometer CORELLI covering a large volume in reciprocal space [39]. Figures 1(c) and 1(d) illustrate the contour map of the neutron scattering pattern obtained at $T = 390$ K and $T = 100$ K. Note that Bragg reflections both in the $(H, K, 0)$ and $(H, 0, L)$ planes are observed due to the twinning of the crystal. Reflections at the $(2n + 1, 0, m)$ position, which corresponds to (integer, 0, half-integer L) in the $P4/nmm$ cell, show considerable intensities and clearly indicate the doubling of the c-axis parameter of the $P4/nmm$ cell. In addition, a close examination of the reflection condition shows a difference between equivalent reflections in the tetragonal space group, implying a lowering of the crystal structure symmetry, which is further confirmed by single crystal x-ray diffraction. Both neutron and x-ray diffraction data can only be modeled and refined using an orthorhombic *Pnma* structure (space group No. 62) instead of a tetragonal $P4/nmm$ structure. For an analysis of structural refinements, see Supplemental Material (SM) Figs. S3 and S4 [40]. In the revised structure, Mn, Yb, and Sb ions are located at the $4c$ sites, all showing a notable displacement in

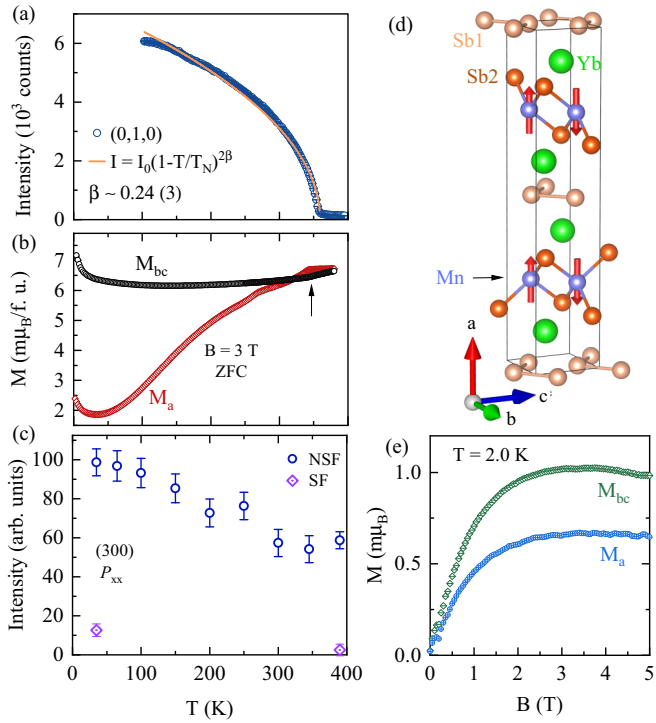

FIG. 2. Temperature dependence of (a) the (0,1,0) reflection peak as a magnetic order parameter, and (b) zero-field-cooled magnetization measured at 3 T. (c) Temperature dependence of the intensity of non-spin-flip and spin-flip scattering process of the (300) reflection peak with the neutron spin aligned along the Q direction. The yellow solid line in (a) represents a fit $I = I_0(1 - T/T_N)^{2\beta}$ to the data. $\beta \sim 0.24$ indicates a quasi-2D nature of magnetism. (d) The refined spin structure of $YbMnSb_2$. The spin carries a dominant a-axis component forming a C-type magnetic structure without a finite c-axis component. (e) The extracted canted FM moment along the bc plane and the a axis after subtracting the magnetic contribution from FM impurity and AFM order.

the basal plane along the c axis [Fig. 1(b)]. The magnitude of the displacement increases as the system is cooled and leads to an enhancement of the characteristic $(2n + 1, 0, m)$ reflections.

After establishing the crystal structure, we now discuss the spin arrangement in $YbMnSb_2$. Figure 2(a) shows the temperature dependence of the peak intensity of the $(0, 1, 0)$ magnetic reflection; it decreases sharply upon warming and becomes a featureless background above $T_N \sim 350$ K, consistent with the transition determined from the magnetization [Fig. 2(b)] and heat capacity (Fig. S2 [40]). This implies a spin structure with a unit cell identical to the nuclear one and moments predominately perpendicular to the basal plane. For magnetic ions located at the $4c$ site with a propagation wave vector $q_m = (0, 0, 0)$, there are eight compatible magnetic space groups. Half of them can be excluded since the spin moments in those configurations are constrained within the basal plane, which contradicts the bulk magnetization data. For the remaining magnetic space groups $Pn'm'a'$, $Pnm'a'$, $Pn'm'a$, and $Pnm'a$, the refinement reveals that the magnetic space group $Pn'm'a'$ provides the most satisfactory description of the diffraction data [Fig. 2(d)]. The Mn spin direction lies along the longest crystal axis, the a axis, with a size of $\sim 3.17(3)\mu_B$ in a collinear C-type AFM arrangement. Although the size of the estimated magnetic moment is similar to a previous report [38], it is smaller than the expected value for a full ordered Mn^{2+} $(5\mu_B)$.

Spin canting, which is allowed from the magnetic space group, could be present since finite intensities were observed at $(2n + 1, 0, 0)$. However, our polarized neutron experiments revealed that a majority of the intensities originate from the nuclear component (as described in Fig. S5 [40]). We measured the intensities of the spin-flip (SF) and non-spin-flip (NSF) scattering processes, in which the spins of the incident neutrons were flipped and remained unchanged, respectively. In the present setup with neutron spin aligned along the Q direction, magnetic and nuclear scattering signals should be separated from each other, and observed in the SF and NSF channels, respectively. Figure 2(c) shows the intensities of the NSF and SF scattering process for the (300) reflection as a function of temperature. As shown in the figure, in the whole temperature range the NSF scattering is much stronger and dominates the SF scattering, and the ratio of the two intensities corresponds to the flipping ratio with an instrumental configuration, suggesting that the origin of these intensities is mainly attributed to the nuclear component. We also estimated the canted moments from the field dependence of the magnetization measurement at different temperatures. In Fig. 2(e), we plot the FM contribution of the canted spin structure to the magnetization after subtracting the contribution of the FM impurity and the AFM ordered state from the magnetization as described in SM [40]. The maximum moment of $\sim 0.001\mu_B$ is comparable to previous reports in $YbMnSb_2$ [38] and $YbMnBi_2$ [19] with a canting angle $\theta \sim 0.018°$. This indicates a negligible canting of the Mn moment away from the a axis.

The orthorhombic $Pnma$ space group enforces a zigzag arrangement of the Sb atoms [as in Fig. 1(b)] along the b axis, leading to a distorted Sb_1 layer similar to $(Ca/Sr/Ba/Eu)MnSb_2$ [9,13,17,18,47]. Despite the in-plane orthorhombicity $(b - c)/c \sim 0.31\%$ in $YbMnSb_2$ being several times smaller than that in the $AMnSb_2$ materials, it is sufficient to drive an anisotropic FS compared to a tetragonal structure. Figures 3(a) and 3(b) show the band structure for $YbMnSb_2$ with the collinear AFM arrangements of Mn spin for orthorhombic $Pnma$ and tetragonal $P4/nmm$ structures using density functional theory (see SM for calculation details [40]) without considering spin-orbit coupling (SOC). The low-energy band structure consists of heavier regular bands near the Γ point and a linearly dispersing Dirac-like band at the X point. The former arises from Mn d orbitals and Sb p orbitals, whereas the latter mainly originates from the Sb p orbitals. When SOC is taken into account, it has little effect on the bands near the Γ point but dramatically increases the gap size at the X point (Fig. S8 in SM [40]). Figures 3(b) and 3(c) compare the BZ of $YbMnSb_2$ in orthorhombic and tetragonal structures, respectively. The FS in the undistorted tetragonal phase is composed of two Dirac-like pockets, one electronlike near the X points and another holelike along the Γ-M line, and a big 3D hole pocket at the Γ point, in good agreement with several previous reports [19,20,30,33]. However, due to the in-plane orthorhombicity, the FS no longer exhibits C_4

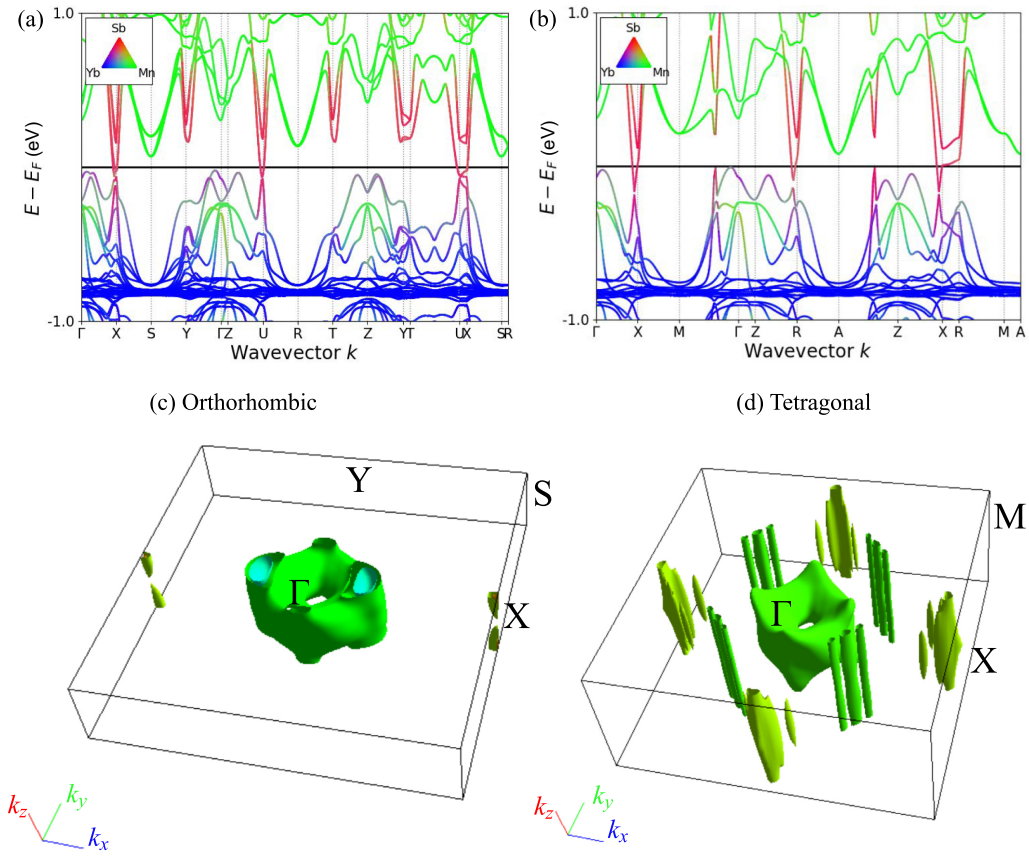

FIG. 3. Momentum-dependent electronic structure of $YbMnSb_2$ in the (a) *Pnma* orthorhombic and (b) *P*4/*nmm* tetragonal structure with collinear AFM arrangement of Mn spins. Color represents the orbital contribution of each atom type as shown in the inset of (a). Brillouin zone of $YbMnSb_2$ for (c) orthorhombic and (d) tetragonal structures showing the FS. For the tetragonal structure E_F is shifted by −50 meV. Due to doubling of the unit cell volume, the BZ volume in the orthorhombic structure becomes half of the tetragonal phase.

rotational symmetry. Moreover, the hole pocket along the Γ-*M* direction becomes gapped and the 3D hole pocket at Γ stretches along the Γ-*X* direction.

Figure 4(a) shows the in-plane resistivity ρ_{xx} and the Hall coefficient R_H at 7 T in the temperature range 2–390 K. With decreasing temperature, ρ_{xx} remains nearly flat down to T_N and decreases sharply below T_N. R_H increases by an order of magnitude from 2.3×10^{-8} m^3/C at 390 K to 2.43×10^{-7} m^3/C at 250 K and decreases slightly on further cooling. The estimated carrier concentration $n_H = |1/R_H e| \sim 2.19 \times 10^{19}$ cm^{-3} at 2 K is comparable with previous reports [29,34], but two orders of magnitude smaller than $YbMnBi_2$ [6]. To obtain more insight, we measured the magnetic field dependence of ρ_{xx} [Fig. 4(b)] and the Hall resistivity ρ_{xy} [Fig. 4(c)] at representative temperatures across the transition. For temperatures above 200 K, the magnetoresistance (MR) increases quadratically in the whole field region, whereas at low temperatures, MR follows quadratic behavior in the low-field region and saturates at higher fields, implying the multiple bands at the FS contribute to the charge transport. Consistent with previous results [29,34], ρ_{xy} remains positive, revealing that holes are dominant charge carriers. ρ_{xy} follows a linear increase up to 7 T for 300 K < T < 390 K but exhibits a concave upward increase below 250 K. Such nonlinear $\rho_{xy}(B)$ indicates that a relatively small number of highly mobile electronlike carriers contribute to the transport property as temperature decreases.

The magnetic field dependence of ρ_{xy} in a multiband system is determined by the interplay of concentration and the mobility of individual carriers. Hence, we analyzed the corresponding $\rho_{xx}(B)$ and $\rho_{xy}(B)$ employing the semiclassical two-band model (Fig. S9 in SM [40]). Figures 4(d) and 4(e) show the thermal evolution of the electron (hole) concentration, n_e (n_h), and electron (hole) mobility, μ_e (μ_h), extracted from the two-band model. The concentration of the hole carriers, n_h, is an order of magnitude larger than the electron-type carriers, n_e, while the mobility of the electronlike carriers, μ_e, is twice that of μ_h. Surprisingly, n_e and μ_e do not show a strong temperature dependence. In contrast, n_h and μ_h display a dramatic temperature dependence as they might be coming from the parabolic bands near the Γ points [in Fig. 3(b)]. Both n_h falls and μ_h rises by two orders of magnitude across the magnetic transition, suggesting that the hole pocket is partially gapped due to band folding as $YbMnSb_2$ transitions from the paramagnetic to AFM ordered state.

To further deduce several important physical parameters related to the FS, we measured ρ_{xx} of another piece of crystal *S*#2 up to 16 T as shown in Fig. 5(a). As the magnetic field exceeds 6 T, prominent Shubnikov–de Hass (SdH) quantum oscillations are detected. Interestingly, a clear splitting

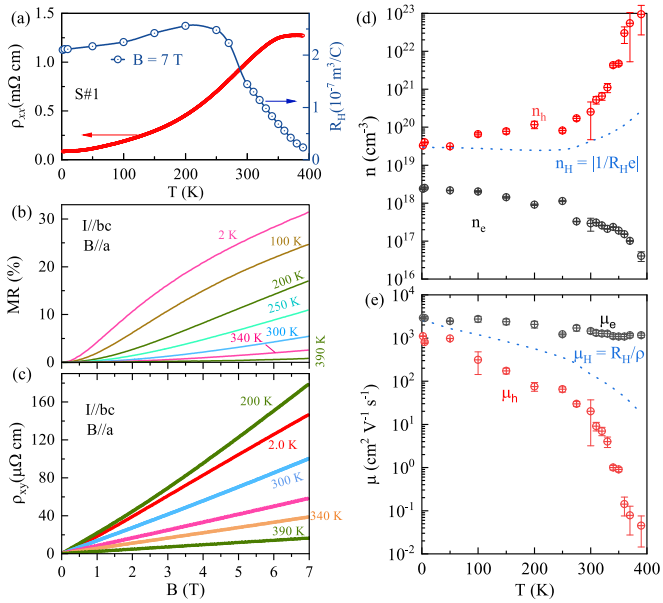

FIG. 4. (a) Temperature dependence of *bc* plane resistivity, ρ_{xx}, and Hall coefficient R_H at 7 T. Magnetic field dependence of (b) magnetoresistance defined as $\{[\rho_{xx}(B) - \rho_{xx}(0)]/\rho_{xx}(0)\} \times 100$, and (c) the Hall resistivity ρ_{xy} in the temperature range 2–390 K. Temperature variation of hole and electron (d) carrier concentration and (e) mobility estimated from the fitting of a two-band model to the MR and Hall data. The blue dotted lines represent the carrier concentration, $n_H = |1/R_H e|$, and mobility, $\mu = R_H/\rho_{xx}$, estimated using the one-band model.

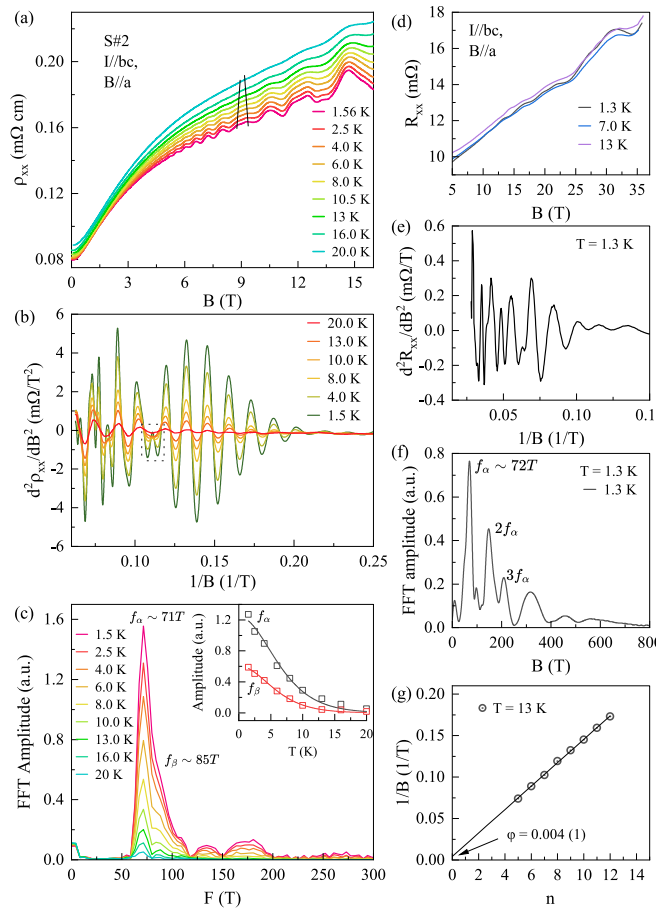

FIG. 5. (a) Field dependence of ρ_{xx} of crystal *S*#2 showing SdH quantum oscillations. (b) The corresponding $d^2\rho_{xx}/dB^2$ vs $1/B$. (c) FFT spectra of the $d^2\rho_{xx}/dB^2$ vs $1/B$ curve at different temperatures. Inset: LK fit [Eq. (2)] to the FFT amplitudes of f_α and f_β. (d) Field dependence of R_{xx} up to 36 T. (e) d^2R_{xx}/dB^2 vs $1/B$ curve for results in (d). (f) The corresponding FFT spectra at $T = 1.3$ K. (g) Landau level fan diagram for f_α constructed using the minimum of $\Delta\rho_{xx}$ at $T = 13$ K.

of the oscillation peak is seen around 9 T, which becomes more prominent at higher magnetic fields. Furthermore, the magnitude of the peak splitting decreases with increasing temperature and disappears above 10 K. The origin of such a splitting of the quantum oscillation peak can be attributed to the spin splitting of Landau levels (LLs) producing two similar oscillation frequencies, which interfere with each other. This becomes more clear from $d^2\rho_{xx}/dB^2$ vs $1/B$ [as shown in Fig. 5(b)], which clearly reveals a beatlike pattern indicating the interference of two similar frequencies. The interference modulates the oscillation amplitude and is described by $R_s = \cos(\pi \Delta E/\hbar\omega_c)$, where ΔE is the size of spin splitting, $\hbar$ is the reduced Planck constant, and ω_c is the cyclotron frequency, which is linear in B. If ΔE is not linear in B, R_s will be field dependent, producing a beating pattern in quantum oscillations as observed in WTe_2 [48], a two-dimensional electron gas [49,50]. Another possibility for the observation of such peak splitting is due to the warped FS arising from the coherent interplanar transport of carriers as reported in Ref. [29]. The corresponding fast Fourier transformation (FFT) reveals two comparable frequencies, $f_\alpha \simeq 71$ T and $f_\beta \simeq 85$ T [Fig. 5(c)]. In previous de Haas–van Alphen [29] and SdH [34] studies of $YbMnSb_2$, only one oscillation frequency f_α has been observed. In contrast, a recent thermopower study revealed multiple frequencies [32]. To sort out the discrepancies, we measured the resistance of another sample up to 36 T as in Fig. 5(d). In Fig. 5(f), we show the FFT spectra of the $d^2\rho_{xx}/dB^2$ vs $1/B$ [Fig. 5(e)]. Consistent with the low-field results, the spectra reveal a single frequency, $f_\alpha \sim 72$ T with multiple higher-order harmonics. Therefore, we believe that f_α and f_β arise from the same Fermi pocket due to the spin splitting of the Landau level or warped FS.

The frequency of quantum oscillation is related to the cross-section area S_F of FS perpendicular to the applied B direction via the Onsager relation, $S_F = (2\pi^2/\phi_0)F$, where ϕ_0 is the single magnetic flux quantum and F is the oscillation frequency. Using this relation, S_F for f_α and f_β is estimated as 0.007 and 0.008 Å^2, respectively, representing tiny FS cross-sectional areas of only 0.3% of the BZ area $(2\pi/b) \times (2\pi/c) = 2.12$ Å^2. We also analyzed the SdH oscillations quantitatively using the Lifshitz-Kosevich (LK) formula [51,52], which predicts the oscillatory component of ρ_{xx}, $\Delta\rho$, as

$$\frac{\Delta\rho}{\rho(0)} \simeq \frac{5}{2}\left(\frac{B}{2F}\right)^{\frac{1}{2}} R_T(T) R_D(T_D) \cos\left[2\pi\left(\frac{F}{B} - \varphi\right)\right], \quad (1)$$

where $\rho(0)$ is the resistivity ρ_{xx} at $B = 0$. The cosine term contains a phase factor $\varphi = \frac{1}{2} - \frac{\phi_B}{2\pi} - \delta$, in which ϕ_B is the Berry's phase and δ is related to FS curvature. $\delta = 0$ for a smooth 2D cylinder, whereas $\delta = \pm 1/8$ for a 3D FS. In

Eq. (1), the Landau level broadening and electron scattering result in two major damping factors, namely, the temperature damping factor $R_T(T)$ and the Dingle factor $R_D(T_D)$, respectively,

$$R_T(T) = \frac{2\pi^2 k_B T m^*}{\hbar e B} \sinh\left(\frac{2\pi^2 k_B T m^*}{\hbar e B}\right) \quad (2)$$

and

$$R_D(T_D) = \exp\left(-\frac{2\pi^2 k_B T_D m^*}{\hbar e B}\right), \quad (3)$$

which are determined by the cyclotron effective mass m^* and the Dingle temperature T_D. Fittings of Eq. (2) to the thermal damping of the FFT amplitude of f_α and f_β [inset of Fig. 5(c)] result in an almost equal $m^* \sim 0.12 m_e$ for f_α and f_β, similar to previous reports [29,34].

In general, the LL fan diagram can be employed to identify the topological nature of quantum oscillation frequencies by plotting the minimum of conductivity against their associated LL index, n [53,54]. In this approach, the in-plane conductivity (σ_{xx}) is converted into longitudinal resistivity ρ_{xx} and transverse (Hall) resistivity ρ_{xy}, using $\sigma_{xx} = \frac{\rho_{xx}}{(\rho_{xx}^2+\rho_{xy}^2)}$. For $YbMnSb_2$, the oscillation component of σ_{xx}, obtained as $\Delta\sigma_{xx}$, is in phase with the $\Delta\rho_{xx}$ (Fig. S10 in SM [40]). Therefore, LL indices can be assigned to the $\Delta\rho$ minimum to construct the LL fan diagram. However, the analysis of such a LL fan diagram becomes problematic if there are multiple frequencies involved or the splitting of the oscillation peak increases dramatically at higher magnetic fields. Therefore, in the present case, to construct a LL fan diagram, we used ρ_{xx} data at $T = 13$ K below 16 T, where LL peak splitting is absent [Fig. 5(g)].

The x intercept of a linear fit to the LL index, n vs $1/B$, provides the accrued ϕ_B when the carrier completes one cyclotron orbit, via the relation $\varphi = 1/2 - \phi_B/2\pi - \delta$. We assume $\delta = 0$, as previous SdH oscillation studies have established the 2D nature of f_α [29,34]. Then $\varphi = 0$ for a topologically nontrivial Berry's phase of π, while a trivial Berry's phase of 0 results in $\varphi = 1/2$. A value of $\varphi = 0.004(1)$ in the present study indicates that the Fermi pocket giving rise to the SdH oscillations is consistent with having a topological origin and Dirac-like dispersion.

IV. CONCLUSION

In summary, we have used neutron and x-ray single crystal diffraction, magnetic susceptibility, and magnetotransport measurements together with complementary band structure calculations to investigate the crystal and magnetic structure as well as the FS topology of $YbMnSb_2$. Both x-ray and neutron diffraction unambiguously revealed that $YbMnSb_2$ crystallizes in an orthorhombic *Pnma* structure. Band structure calculations revealed a reduced BZ and more anisotropic FS of $YbMnSb_2$ compared to $YbMnBi_2$ because of in-plane orthorhombicity. The FS of $YbMnSb_2$ consisting of an anisotropic heavier regular band and a linearly dispersing Dirac-like band no longer exhibits C_4 rotational symmetry as in undistorted $YbMnBi_2$. An analysis of SdH quantum oscillation reveals a nontrivial nature of a tiny Fermi pocket consistent with Dirac-like energy-momentum dispersion.

ACKNOWLEDGMENTS

We are thankful to S. Nagasaki, D. Hamane, T. Miyake, and T. Masuda for technical help during experiments. We also gratefully acknowledge fruitful discussion with K. Matsubayashi, P. Shahi and Branton Campbell. This work was financially supported by the JSPS KAKENHI Grants No. JP19H00648 and No. 23H04862. A portion of this research used resources at HFIR and SNS, DOE Office of Science User Facilities operated by the Oak Ridge National Laboratory. The preliminary polarized neutron scattering experiment at JRR-3 was carried out along Proposal No. 22401. The beam time was allocated to CORELLI on Proposal No. IPTS-29639 and to PTAX on Proposal No. IPTS-31142. A.M. acknowledges support from ANRF erstwhile SERB (Grant No. SRG/2023/001718) and DST-FIST, India. The Fermi surfaces and band structure figures were respectively plotted using FERMISURFER [55] and PYMATGEN [56].

[1] K. Wang, D. Graf, H. Lei, S. W. Tozer, and C. Petrovic, Quantum transport of two-dimensional Dirac fermions in $SrMnBi_2$, Phys. Rev. B **84**, 220401(R) (2011).

[2] K. Wang, D. Graf, L. Wang, H. Lei, S. W. Tozer, and C. Petrovic, Two-dimensional Dirac fermions and quantum magnetoresistance in $CaMnBi_2$, Phys. Rev. B **85**, 041101(R) (2012).

[3] J. Park, G. Lee, F. Wolff-Fabris, Y. Y. Koh, M. J. Eom, Y. K. Kim, M. A. Farhan, Y. J. Jo, C. Kim, J. H. Shim, and J. S. Kim, Anisotropic Dirac fermions in a Bi square net of $SrMnBi_2$, Phys. Rev. Lett. **107**, 126402 (2011).

[4] Y. J. Jo, J. Park, G. Lee, Man J. Eom, E. S. Choi, J. H. Shim, W. Kang, and J. S. Kim, Valley-polarized interlayer conduction of anisotropic Dirac fermions in $SrMnBi_2$, Phys. Rev. Lett. **113**, 156602 (2014).

[5] J. Y. Liu, J. Hu, D. Graf, T. Zou, M. Zhu, Y. Shi, S. Che, S. M. A. Radmanesh, C. N. Lau, L. Spinu, H. B. Cao, X. Ke, and Z. Q. Mao, Unusual interlayer quantum transport behavior caused by the zeroth Landau level in $YbMnBi_2$, Nat. Commun. **8**, 646 (2017).

[6] A. Wang, I. Zaliznyak, W. Ren, L. Wu, D. Graf, V. O. Garlea, J. B. Warren, E. Bozin, Y. Zhu, and C. Petrovic, Magnetotransport study of Dirac fermions in $YbMnBi_2$ antiferromagnet, Phys. Rev. B **94**, 165161 (2016)

[7] Y. Feng, Z. Wang, C. Chen, Y. Shi, Z. Xie, H. Yi, A. Liang, S. He, J. He, Y. Peng, X. Liu, Y. Liu, L. Zhao, G. Liu, X. Dong, J. Zhang, C. Chen, Z. Xu, X. Dai, Z. Fang, and X. J. Zhou, Strong anisotropy of Dirac cones in $SrMnBi_2$ and $CaMnBi_2$ revealed by angle-resolved photoemission spectroscopy, Sci. Rep. **4**, 5385 (2016).

[8] J. Y. Liu, J. Hu, Q. Zhang, D. Graf, H. B. Cao, S. M. A. Radmanesh, D. J. Adams, Y. L. Zhu, G. F. Cheng, X. Liu, W. A. Phelan, J. Wei, M. Jaime, F. Balakirev, D. A. Tennant, J. F. DiTusa, I. Chiorescu, L. Spinu, and Z. Q. Mao, A magnetic

topological semimetal $Sr_{1-y}Mn_{1-z}Sb_2$ ($y, z < 0.1$), Nat. Mater. **16**, 905 (2017).

[9] J. B. He, Y. Fu, L. X. Zhao, H. Liang, D. Chen, Y. M. Leng, X. M. Wang, J. Li, S. Zhang, M. Q. Xue, C. H. Li, P. Zhang, Z. A. Ren, and G. F. Chen, Quasi-two-dimensional massless Dirac fermions in $CaMnSb_2$, Phys. Rev. B **95**, 045128 (2017).

[10] A. Zhang, C. Liu, C. Yi, G. Zhao, T.-L. Xia, J. Ji, Y. Shi, R. Yu, X. Wang, C. Chen, and Q. Zhang, Interplay of Dirac electrons and magnetism in $CaMnBi_2$ and $SrMnBi_2$, Nat. Commun. **7**, 13833 (2016).

[11] S. Huang, J. Kim, W. A. Shelton, E. W. Plummer, and R. Jin, Nontrivial Berry phase in magnetic $BaMnSb_2$ semimetal, Proc. Natl. Acad. Sci. USA **114**, 6256 (2017).

[12] J. Liu, J. Hu, H. Cao, Y. Zhu, A. Chuang, D. Graf, D. J. Adams, S. M. A. Radmanesh, L. Spinu, I. Chiorescu, and Z. Mao, Nearly massless Dirac fermions hosted by Sb square net in $BaMnSb_2$, Sci. Rep. **6**, 30525 (2016).

[13] C. Yi, S. Yang, M. Yang, L. Wang, Y. Matsushita, S. Miao, Y. Jiao, J. Cheng, Y. Li, K. Yamaura, Y. Shi, and J. Luo, Large negative magnetoresistance of a nearly Dirac material: Layered antimonide $EuMnSb_2$, Phys. Rev. B **96**, 205103 (2017).

[14] A. F. May, M. A. McGuire, and B. C. Sales, Effect of Eu magnetism on the electronic properties of the candidate Dirac material $EuMnBi_2$, Phys. Rev. B **90**, 075109 (2014).

[15] S. Borisenko, D. Evtushinsky, Q. Gibson, A. Yaresko, K. Koepernik, T. Kim, M. Ali, J. van den Brink, M. Hoesch, A. Fedorov, E. Haubold, Y. Kushnirenko, I. Soldatov, R. Schäfer, and R. J. Cava, Time-reversal symmetry breaking type-II Weyl state in $YbMnBi_2$, Nat. Commun. **10**, 3424 (2019).

[16] H. Masuda, H. Sakai, M. Tokunaga, Y. Yamasaki, A. Miyake, J. Shiogai, S. Nakamura, S. Awaji, A. Tsukazaki, H. Nakao, Y. Murakami, T. Arima, Y. Tokura, and S. Ishiwata, Quantum Hall effect in a bulk antiferromagnet $EuMnBi_2$ with magnetically confined two-dimensional Dirac fermions, Sci. Adv. **2**, e1501117 (2016).

[17] J. Y. Liu, J. Yu, J. L. Ning, H. M. Yi, L. Miao, L. J. Min, Y. F. Zhao, W. Ning, K. A. Lopez, Y. L. Zhu *et al.*, Spin-valley locking and bulk quantum Hall effect in a noncentrosymmetric Dirac semimetal $BaMnSb_2$, Nat. Commun. **12**, 4062 (2021)

[18] H. Sakai, H. Fujimura, S. Sakuragi, M. Ochi, R. Kurihara, A. Miyake, M. Tokunaga, T. Kojima, D. Hashizume, T. Muro *et al.*, Bulk quantum Hall effect of spin-valley coupled Dirac fermions in the polar antiferromagnet $BaMnSb_2$, Phys. Rev. B **101**, 081104(R) (2020).

[19] Y. Pan, C. Le, B. He, S. J. Watzman, M. Yao, J. Gooth, J. P. Heremans, Y. Sun, and C. Felser, Giant anomalous Nernst signal in the antiferromagnet $YbMnBi_2$, Nat. Mater. **21**, 203 (2022).

[20] C. Le, C. Felser, and Y. Sun, Design strong anomalous Hall effect via spin canting in antiferromagnetic nodal line materials, Phys. Rev. B **104**, 125145 (2021).

[21] X. Li, A. H. MacDonald, and H. Chen, Quantum anomalous Hall effect through canted antiferromagnetism, arXiv:1902.10650.

[22] P.-J. Guo, Z.-X. Liu, and Z.-Y. Lu, Quantum anomalous Hall effect in antiferromagnetism, npj Comput. Mater. **9**, 70 (2023).

[23] X.-S. Ni, C.-Q. Chen, D.-X. Yao, and Y. Hou, Origin of the type-II Weyl state in topological antiferromagnetic $YbMnBi_2$, Phys. Rev. B **105**, 134406 (2022).

[24] R. Yang, M. Corasaniti, C. C. Le, Z. Y. Liao, A. F. Wang, Q. Du, C. Petrovic, X. G. Qiu, J. P. Hu, and L. Degiorgi, Spin-canting-induced band reconstruction in the Dirac material $Ca_{1-x}Na_xMnBi_2$, Phys. Rev. Lett. **124**, 137201 (2020).

[25] A. Sapkota, L. Classen, M. B. Stone, A. T. Savici, V. O. Garlea, A. Wang, J. M. Tranquada, C. Petrovic, and I. A. Zaliznyak, Signatures of coupling between spin waves and Dirac fermions in $YbMnBi_2$, Phys. Rev. B **101**, 041111(R) (2020).

[26] J.-R. Soh, H. Jacobsen, B. Ouladdiaf, A. Ivanov, A. Piovano, T. Tejsner, Z. Feng, H. Wang, H. Su, Y. Guo, Y. Shi, and A. T. Boothroyd, Magnetic structure and excitations of the topological semimetal $YbMnBi_2$, Phys. Rev. B **100**, 144431 (2019).

[27] X. Hu, A. Sapkota, Z. Hu, A. T. Savici, A. I. Kolesnikov, J. M. Tranquada, C. Petrovic, and I. A. Zaliznyak, Coupling of magnetism and Dirac fermions in $YbMnSb_2$, Phys. Rev. B **107**, L201117 (2023).

[28] S. M. Tobin, J.-R. Soh, H. Su, A. Piovano, A. Stunault, J. A. Rodríguez-Velamazán, Y. Guo, and A. T. Boothroyd, Magnetic excitations in the topological semimetal $YbMnSb_2$, Phys. Rev. B **107**, 195146 (2023).

[29] Y.-Y. Wang, Y.-Y. Wang, S. Xu, L.-L. Sun, and T.-L. Xia, Quantum oscillations and coherent interlayer transport in a new topological Dirac semimetal candidate $YbMnSb_2$, Phys. Rev. Mater. **2**, 021201(R) (2018).

[30] Y. Pan, F.-R. Fan, X. Hong, B. He, C. Le, W. Schnelle, Y. He, K. Imasato, H. Borrmann, C. Hess, B. Büchner, Y. Sun, C. Fu, G. J. Snyder, and C. Felser, Thermoelectric properties of novel semimetals: A case study of $YbMnSb_2$, Adv. Mater. **33**, 2003168 (2021).

[31] S. Baranets and S. Bobev, Transport properties and thermal behavior of $YbMnSb_2$ semimetal above room temperature, J. Solid State Chem. **303**, 122467 (2021).

[32] S. Xu, C. Jiang, S.-X. Li, J.-J. Mi, Z. Li, T.-L. Xia, Q. Tao, and Z.-A. Xu, Large Nernst effect and possible temperature-induced Lifshitz transition in topological semimetal $YbMnSb_2$, Phys. Rev. B **107**, 245138 (2023).

[33] Z. Qiu, C. Le, Z. Liao, B. Xu, R. Yang, J. Hu, Y. Dai, and X. Qiu, Observation of a topological nodal-line semimetal in $YbMnSb_2$ through optical spectroscopy, Phys. Rev. B **100**, 125136 (2019)

[34] R. Kealhofer, S. Jang, S. M. Griffin, C. John, K. A. Benavides, S. Doyle, T. Helm, P. J. W. Moll, J. B. Neaton, J. Y. Chan, J. D. Denlinger, and J. G. Analytis, Observation of a two-dimensional Fermi surface and Dirac dispersion in $YbMnSb_2$, Phys. Rev. B **97**, 045109 (2018).

[35] T. M. Michels-Clark, A. T. Savici, V. E. Lynch, X. Wang, and C. M. Hoffmann, Expanding Lorentz and spectrum corrections to large volumes of reciprocal space for single-crystal time-of-flight neutron diffraction, J. Appl. Crystallogr. **49**, 497 (2016).

[36] A. S. Wills, A new protocol for the determination of magnetic structures using simulated annealing and representational analysis (SARAh), Phys. B: Condens. Matter **276–278**, 680 (2000).

[37] J. Rodríguez-Carvajal, Recent advances in magnetic structure determination by neutron powder diffraction, Phys. B: Condens. Matter **192**, 55 (1993).

[38] J.-R. Soh, S. M. Tobin, H. Su, I. Zivkovic, B. Ouladdiaf, A. Stunault, J. A. Rodríguez-Velamazán, K. Beauvois, Y. Guo, and A. T. Boothroyd, Magnetic structure of the topological semimetal $YbMnSb_2$, Phys. Rev. B **104**, L161103 (2021).

[39] F. Ye, Y. Liu, R. Whitfield, R. Osborn, and S. Rosenkranz, Implementation of cross correlation for energy discrimination on the time-of-flight spectrometer CORELLI, J. Appl. Crystallogr. **51**, 315 (2018).

[40] See Supplemental Material at http://link.aps.org/supplemental/10.1103/lk8w-7hkj for details pertaining to polarized microscopy, heat capacity, Rietveld refinements, polarized neutron scattering, DFT result with SOC, estimation of the spin canting moment, and analysis of magnetotransport data using semiclassical two-band model, which includes Refs. [41–46].

[41] H. Yoshizawa, H. Sakai, M. Kondo, M. Ochi, K. Kuroki, N. Hanasaki, and J. Fujioka, In-plane anisotropic charge dynamics in the layered polar Dirac semimetal $BaMnSb_2$, Phys. Rev. B **105**, L241110 (2022).

[42] D. C. Johnston, The puzzle of high temperature superconductivity in layered iron pnictides and chalcogenides, Adv. Phys. **59**, 803 (2010).

[43] G. Kresse and J. Furthmüller, Efficient iterative schemes for *ab initio* total-energy calculations using a plane-wave basis set, Phys. Rev. B **54**, 11169 (1996).

[44] J. P. Perdew, K. Burke, and M. Ernzerhof, Generalized gradient approximation made simple, Phys. Rev. Lett. **77**, 3865 (1996).

[45] P. E. Blöchl, Projector augmented-wave method, Phys. Rev. B **50**, 17953 (1994).

[46] S. L. Dudarev, G. A. Botton, S. Y. Savrasov, C. J. Humphreys, and A. P. Sutton, Electron-energy-loss spectra and the structural stability of nickel oxide: An LSDA+U study, Phys. Rev. B **57**, 1505 (1998).

[47] D. Gong, S. Huang, F. Ye, X. Gui, J. Zhang, W. Xie, and R. Jin, Canted Eu magnetic structure in $EuMnSb_2$, Phys. Rev. B **101**, 224422 (2020).

[48] R. Bi, Z. Feng, X. Li, J. Niu, J. Wang, Y. Shi, D. Yu, and X. Wu, Spin zero and large Landé g-factor in WTe_2, New J. Phys. **20**, 063026 (2018).

[49] S. A. Studenikin, P. T. Coleridge, G. Yu, and P. J. Poole, Electron spin–orbit splitting in a InGaAs/InP quantum well studied by means of the weak-antilocalization and spin-zero effects in tilted magnetic fields, Semicond. Sci. Technol. **20**, 1103 (2005).

[50] Y. S. Gui, C. R. Becker, J. Liu, V. Daumer, V. Hock, H. Buhmann, and L. W. Molenkamp, Interplay of Rashba, Zeeman and Landau splitting in a magnetic two-dimensional electron gas, Europhys. Lett. **65**, 393 (2004).

[51] G. Landwehr and E. I. Rashba, *Landau Level Spectroscopy: Modern Problems in Condensed Matter Sciences* (North-Holland, Amsterdam, 1991), Vol. 27.2.

[52] D. Shoenberg, *Magnetic Oscillations in Metals* (Cambridge University Press, Cambridge, UK, 1984).

[53] J. Xiong, Y. Luo, Y. Khoo, S. Jia, R. J. Cava, and N. P. Ong, High-field Shubnikov–de Haas oscillations in the topological insulator Bi_2Te_2Se, Phys. Rev. B **86**, 045314 (2012).

[54] A. A. Taskin and Y. Ando, Berry phase of nonideal Dirac fermions in topological insulators, Phys. Rev. B **84**, 035301 (2011).

[55] M. Kawamura, FermiSurfer: Fermi-surface viewer providing multiple representation schemes, Comput. Phys. Commun. **239**, 197 (2019).

[56] S. Ping Ong, W. D. Richards, A. Jain, G. Hautier, M. Kocher, S. Cholia, D. Gunter, V. Chevrier, K. A. Persson, and G. Ceder, Python materials genomics (pymatgen): A robust, open-source python library for materials analysis, Comput. Mater. Sci. **68**, 314 (2013).